Relationship Between the Strengthening Effect and the Morphology of Precipitates in Al–7.4Zn–1.7Mg–2.0Cu Alloy

Xiubo Yang · Jizi Liu · Jianghua Chen · Caiyun Wan · Lei Fang · Ping Liu · Cuilan Wu

Abstract   The morphological evolution of the precipitates in Al–7.4Zn–1.7Mg–2.0Cu (wt%) alloy was studied by high-resolution transmission electron microscopy (HRTEM). Statistics reveal that the hardness of the alloy changes accordingly with the change of the average thickness–diameter ratio of precipitates. The GPII zones are mainly responsible for the first and also the highest hardness peak. They grow in diameter and keep 7-atomic-layer in thickness. Once the thickness changes, the phase transformation from GPII zone to η' or η-precursor would occur. The resultant metastable η' and η-precursor precipitates grow in both diameter and thickness, but much faster in the former. After the first hardness peak, the metastable η' precipitates and η-precursor, coexisting with part of GPII zones, are counted as the main hardening precipitates.

KEY WORDS: Aluminum alloys; Precipitates; Age hardening; Electron microscopy; Morphology
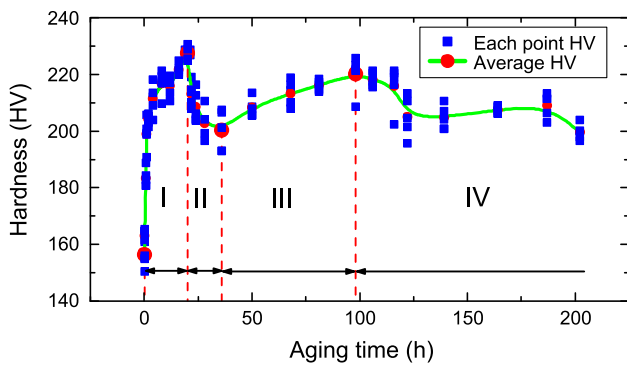
1 Introduction

Al–Zn–Mg–Cu alloys are used widely as structural materials in the aerospace industries due to their ultra-high strength and other good properties [1–3]. As age-hardenable alloys, their enviable strength is in most cases associated with nanoscale precipitates, which are produced during natural or artificial aging of the supersaturated solid solution [4, 5]. Generally, for most of the Al–Zn–Mg–(Cu) alloys, the widely accepted precipitation sequence is [6–10]

X. Yang · J. Liu (✉) · J. Chen · C. Wan · L. Fang · P. Liu · C. Wu
College of Materials Science & Engineering, Hunan University, Changsha 410082, China
e-mail: jzliu123@hnu.edu.cn

J. Liu · J. Chen · C. Wu
Hunan Province Key Laboratory for Spray Deposition Technology and Application, Hunan University, Changsha 410082, China

solid solution $\rightarrow$ GP (I, II) zones $\rightarrow$ metastable $\eta' \rightarrow$ stable η-MgZn$_2$. In an artificially aged AA7108-alloy, two types of GP zones (GPI and GPII) with different structures were confirmed [11]. GPI zones are spherical with AuCu(I)-type sub-units [11, 12], while GPII zones are disk-like with a wide plane lying on $\{111\}_{Al}$ [11]. They both are fully coherent with the matrix and are regarded as the nuclei of the metastable η' phase, although nucleation of the η' phase remains to be controversial [13–15]. The metastable η' phase with platelet morphology has usually been considered to have a hexagonal structure with the lattice parameters $a = 0.496$ nm and $c = 6d_{111Al} = 1.402$ nm, and these are several different atomic models having been reported [13, 16]. The rod-like η phase is incoherent and exhibits numerous crystallographic orientation relationships with the matrix [6]. GP zones and η' precipitates are well accepted to be responsible for the high strength of these alloys, although the amount of their contribution is still a subject of debate [8, 17, 18]. The η-phase, in contrast, leads to a decrease in strength. Besides, our previous work found another hardening phase, i.e., η-precursor [19]. It has a typical morphology of hexagonal
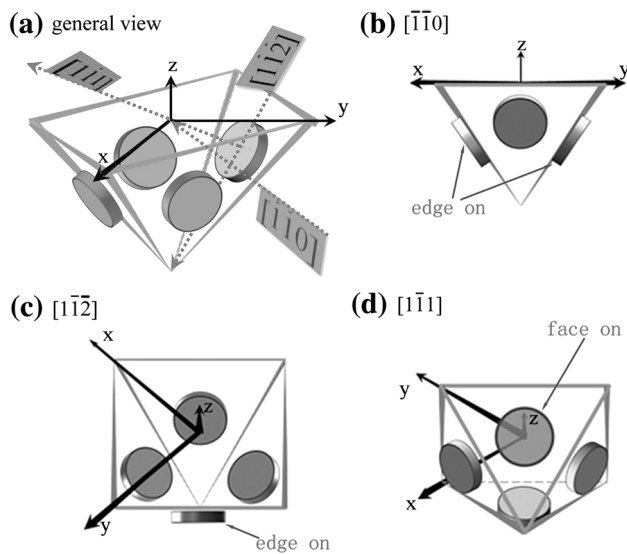
**Fig. 1** Hardness–time curve of samples aged at 120 °C

Fig. 2 Schematic of GPII zones in Al matrix: **a** 3D view of GPII zones lying on four equivalent {111} planes of Al matrix; **b** projection of GPII zones along $[\bar{1}\bar{1}0]_{Al}$; **c** projection of GPII zones along $[1\bar{1}\bar{2}]_{Al}$; **d** projection of GPII zones along $[1\bar{1}1]_{Al}$

platelet and the same orientation relationship as that of η' phase with the matrix: $(0001)_p//\{111\}_{Al}$, $11-\bar{2}0_p//\langle112\rangle_{Al}$, $10-\bar{1}0_p//(110)_{Al}$, where p represents η' or η-precursor precipitates.

Aging treatments and alloy composition engineering are reported extensively to control the type, the size, and the number density of the precipitates with the objective of achieving optimum properties [20–26]. The features of the precipitates (including morphology, orientation, and distribution, and so on) have long been recognized as potential important factors determining the strength of alloys. If the particles are strong enough to stop the dislocation from slicing, the quantitative effects on the yield strength of alloys can be usually described by appropriate versions of the Orowan equation [27]. However, for most of the precipitation-hardened alloys, their metastable nano-precipitates can be sliced by dislocation. In this regard, much interest has been attracted to study the quantitative relationship between phases and mechanical properties during aging treatments [28]. As mentioned above, there are four types of precipitates in age-hardening Al–Zn–Mg–(Cu) alloys: GPI zones, GPII zones, η' and η-precursor. Among these, GPI zones are usually regarded as solute clusters resulted from natural aging and exist at the initial stage of artificial aging, while the others all contribute to the hardness peak platform. Up to now, much interest has been paid to research the structures of these strengthening precipitates and their qualitative effects on the properties, while little was paid on the morphological evolution of these precipitates and their size effects.

In this study, the quantitative relationship between the precipitate size and the hardness of alloy was studied through detailed HRTEM investigations based on statistics. It reveals that the hardness of alloy changes along with the aspect ratio (diameter–thickness ratio) of the precipitates.
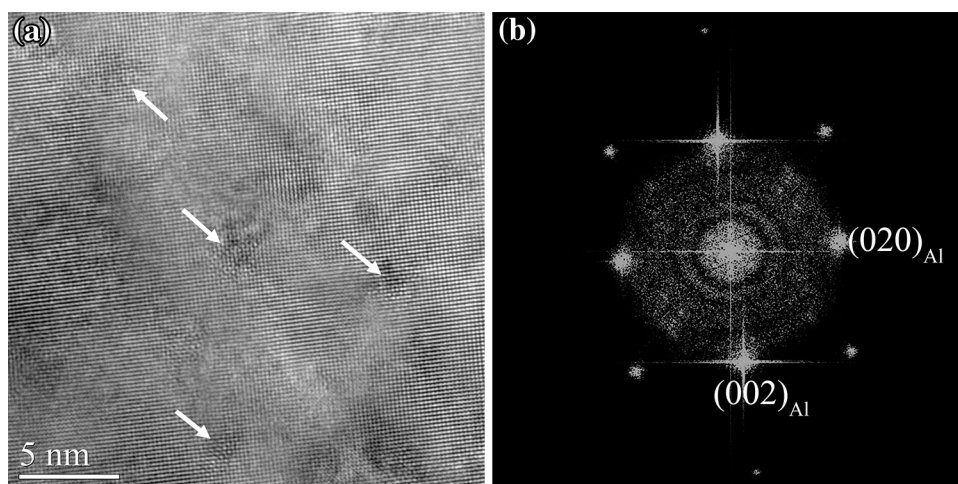
Fig. 3 HRTEM image **a**, corresponding FFT pattern **b** taking along $[001]_{Al}$ zone axis from sample aged at 120 °C for 1 h
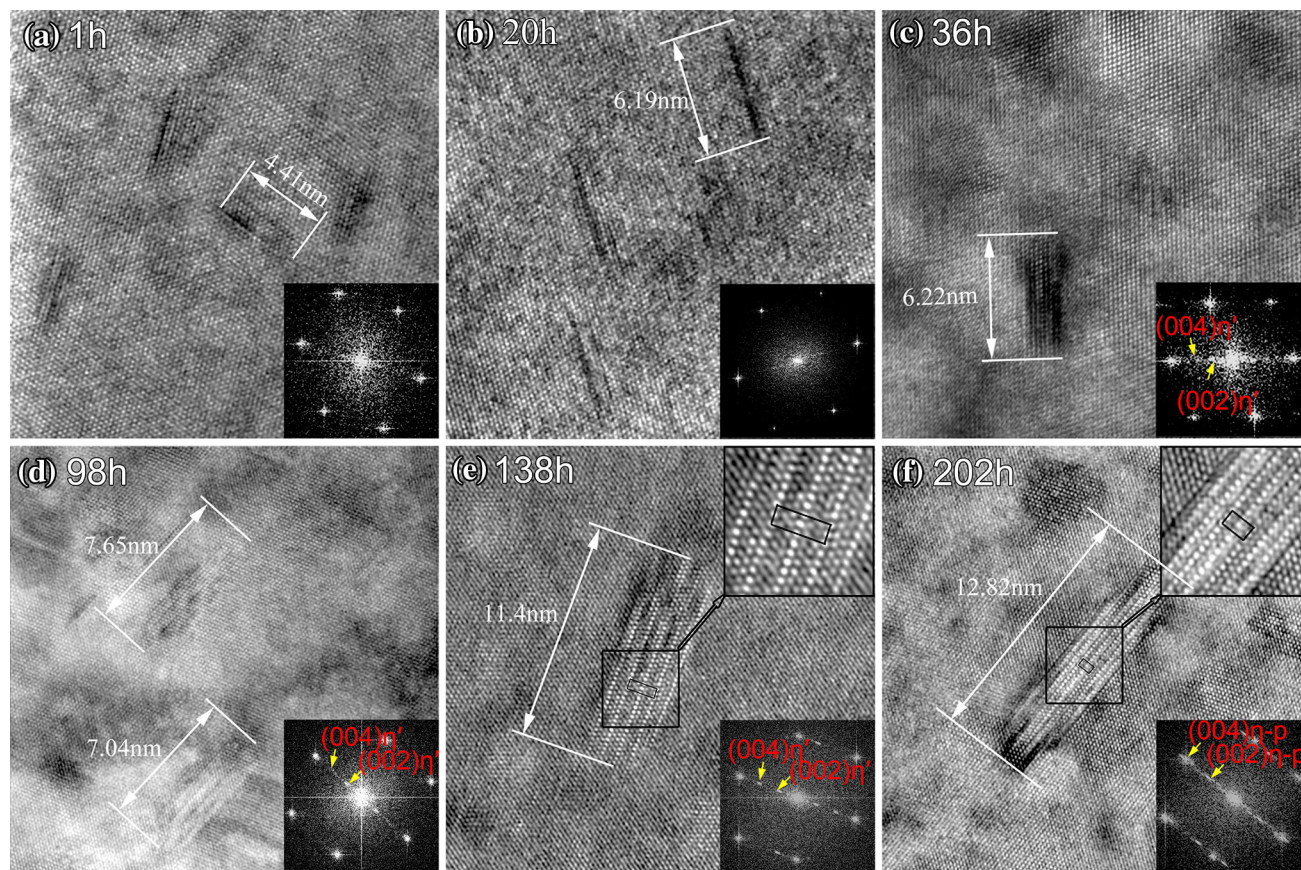
Fig. 4 Typical HRTEM images of precipitates viewed along $\langle 110\rangle_{Al}$ zone axis in samples aged at 120 °C for 1 h **a**, 20 h **b**, 36 h **c**, 98 h **d**, 138 h **e**, 202 h **f**

The relationship between morphological evolution of the precipitates and phase transformation is also investigated in details during aging.

2 Experimental

Al–7.4Zn–1.7Mg–2.0Cu (wt%) alloy ingot was hot extruded into a bar shape with diameter of 12 mm. Then, the bar was cut transversely into disks with thickness of 0.5 mm by wire electrical discharge machining (WEDM). All disk samples were first solution heat-treated at 465 °C for 1 h in the box furnace and then water quenched to room temperature. Subsequently, the quenched samples were aged at 120 °C in oil bath for 5 min to 202 h. The specimens for HRTEM observation were mechanically thinned down to $\sim$80 µm and then electro-polished using a twinjet in methanol solution mixed with 30% nitric acid at −20 to −30 °C and a voltage of 11–14 V. HRTEM observations were performed using a JEOL JEM-3010 microscope operated at 300 kV. The hardness measurements were carried out with a Vickers Hardness tester with an applied

load of 9.8 N and a dwelling time of 15 s. Each hardness value was obtained by averaging five measurements.

3 Results

Figure 1 shows the result of the hardness measurements labeled by blue dots. The red spots denote the average hardness values. The hardness–time curve can be roughly divided into four regions. In region I, the hardness increases rapidly, and the highest hardness is achieved by aging for 20 h; In region II, after the first peak, the hardness decreases to some extent; In region III, the hardness increases slowly and then reaches the second peak; In region IV, after then the hardness decreases slowly again and there is no longer any increasing.

As well known, GPI zones, GPII zones, η′ and η-precursor are well accepted as hardening precipitates in Al–Zn–Mg–(Cu) alloys. GPII zones, η′ and η-precursor have similar platelet morphology and the same orientation relationship with matrix. As an example, the relationship between GPII zones and the matrix is schematically shown
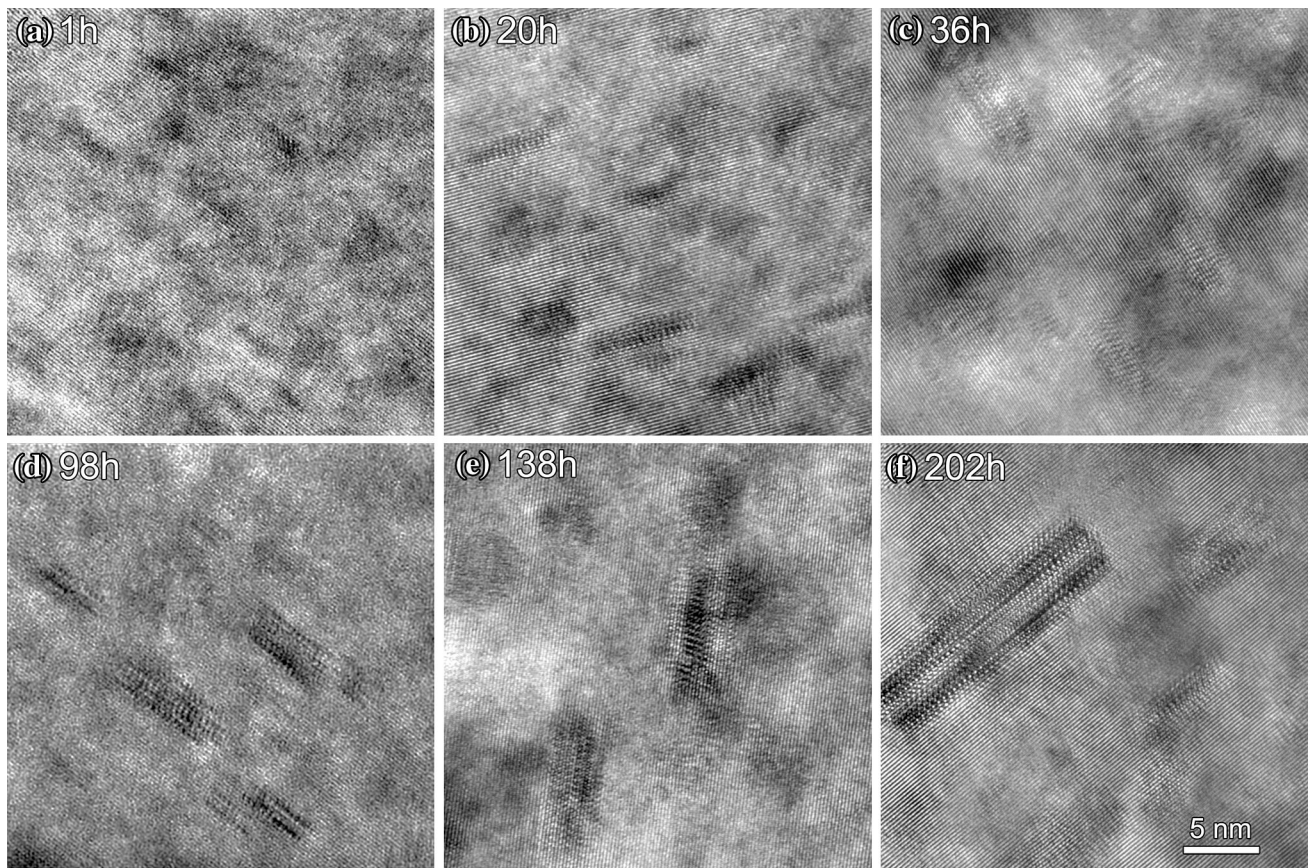
Fig. 5 Typical HRTEM images of precipitates viewed along <112>$_{Al}$ zone axis in samples aged at 120 °C for 1 h **a**, 20 h **b**, 36 h **c**, 98 h **d**, 138 h **e**, 202 h **f**

in Fig. 2. There are four equivalent {111} planes in Al matrix, indicated as four side faces of a rectangular pyramid in Fig. 2a. According to the fixed orientation relationship, the disk planes (wide plane) of the precipitates lie on {111}$_{Al}$. In theory, the number of precipitates on each of {111} planes is equal. Therefore, in <110>$_{Al}$ projection (Fig. 2b), half of precipitates are rectangular and the other half are elliptic; in the <112>$_{Al}$ projection (Fig. 2c), 1/4 precipitates are rectangular and 3/4 precipitates are elliptic; and in the <111>$_{Al}$ projection (Fig. 2d), 1/4 precipitates are circular and 3/4 precipitates are elliptic. It cautions us not to distinguish simply the elliptic precipitates into spherical GPI zones. Obviously, it is better to observe GPII zones, η′ and η-precursor precipitates along <110>$_{Al}$ and <112>$_{Al}$ zone axes. In order to differentiate η-precursor from η′ by morphology, it is necessary to observe the precipitates along <111>$_{Al}$ zone axis. GPI zones are better to be observed along <001>$_{Al}$ zone axis.

Figure 3 shows HRTEM image and corresponding fast Fourier transform (FFT) pattern taking along [001]$_{Al}$ zone axis from the sample aged at 120 °C for 1 h. Some square-round precipitates were observed in Fig. 3a, the corresponding FFT pattern is shown in Fig. 3b. As reported by

Berg et al. [11], the strongest diffuse spots from GPI zones appeared at the positions 1, 1/4, 0$_{Al}$ and 1, 7/4, 0$_{Al}$. However, compared with Fig. 3b, the characteristic diffraction spots for GPI zones are not found. So, the square-round contrast is likely from the projection of GPII zones along [001]$_{Al}$. Although GPI zones are reported to be formed in the temperature range from room temperature to 140–150 °C, they usually exist in the initial stage of artificial aging at elevated temperature and evolve into GPII zones in the later stage. In the current experiment, GPI zones are not observed in the samples aged for 1 h, meaning that the transformation from GPI zones to GPII zones has been achieved in the first one hour at 120 °C. Therefore, GPI zones have little contribution to the hardness peak.

Figure 4 shows HRTEM images of the precipitates viewed along <110>$_{Al}$ zone axis in the samples aged at 120 °C for different typical time (according to the hardness curve). In the sample aged for 1 h, many platelet traces are observed (Fig. 4a). These precipitates appear edge-on as thin layers on {111}-planes, which approximate 7-atomic-layers thick and 3–5-nm wide. These crystallographic features fit to the definitions of GPII zones suggested by
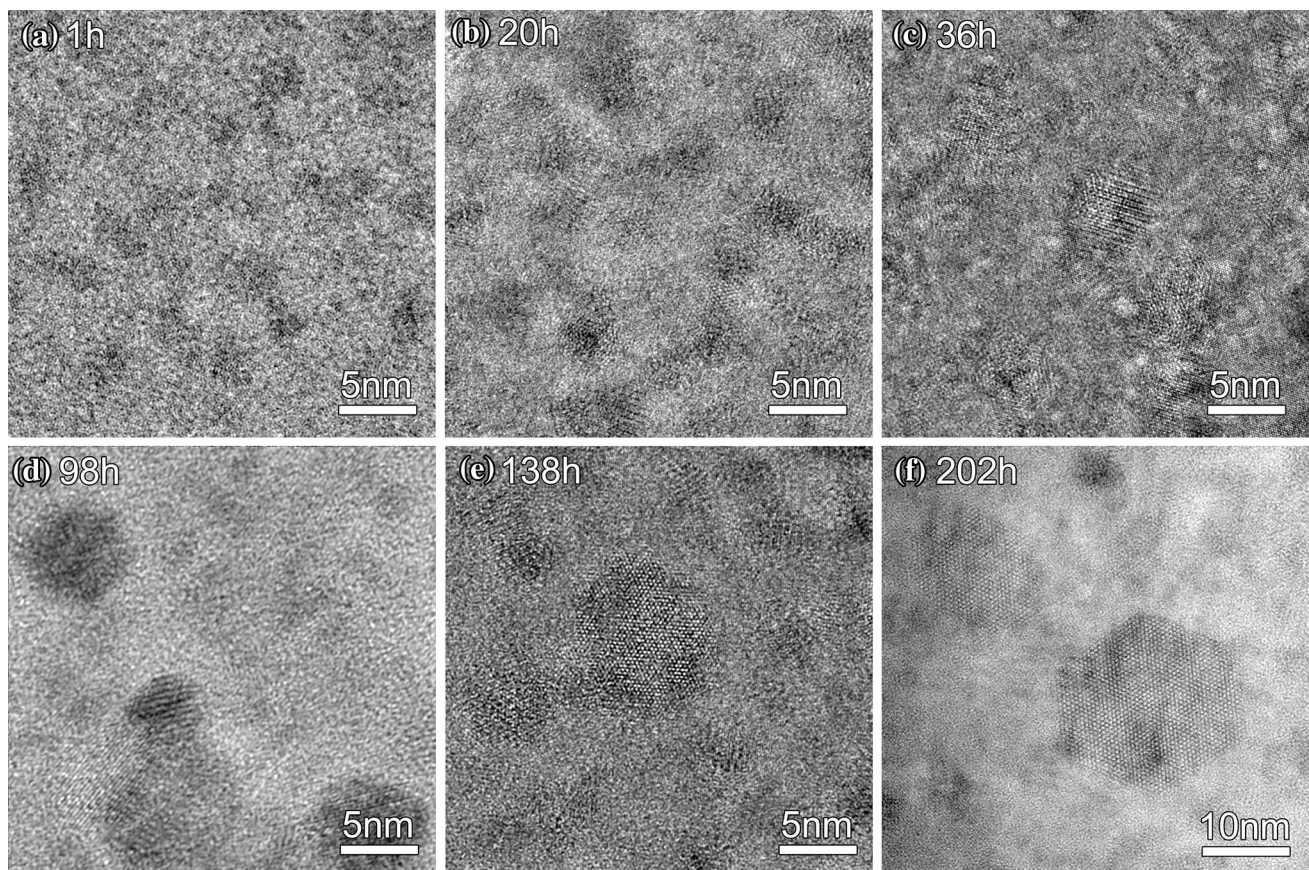
Fig. 6 Typical HRTEM images of precipitates viewed along <111>$_{Al}$ zone axis in samples aged at 120 °C for 1 h **a**, 20 h **b**, 36 h **c**, 98 h **d**, 138 h **e**, 202 h **f**

Refs. [11, 19]. GPII zones are fully coherent with the matrix, and formed by zinc atoms instead of some aluminum atoms. Dark or bright contrast on both sides of the zones indicates an associated strain field resulting from atomic size effect. As time goes on, a comparison of Fig. 4a with Fig. 4b shows that precipitates grow as long as 6–7 nm in their diameter but still keep the approximate 7-atomic-layers thickness with aging time up to 20 h (corresponding to the first peak on hardness curve). So far, no stronger diffuse spots have been observed by FFT pattern (as insets in Fig. 4a, b) of the precipitates, except for indistinct streaks in between the transmission spot (000) and diffraction spot (111)$_{Al}$. For the sample aged for 36 h (corresponding to the first peak valley on hardness curve), the thickness of precipitates reaches up to 10-atomic-layers, as shown in Fig. 4c, and the diameter of precipitates is still 6–7 nm. Prolonging the aging time, these precipitates grow along with the thickness and the diameter in turn slowly. After 98 h aging (corresponding to the second peak on hardness curve), many precipitates with 7–8 nm in diameter and 10—13-atomic-layers in thickness were observed in the age-hardening sample, as shown in Fig. 4d.

With increasing aging time to 138 h (Fig. 4e), some precipitates grow along their diameter fast up to 11–12 nm. In the stage of aging time from 36 to 138 h, the diffuse spots in between the (000) and (111)$_{Al}$ in the reciprocal lattice become stronger and stronger, which indicates that the structure of the precipitates become more mature. In Fig. 4e, the unit cell of η′ precipitates can be drawn out as boxed without any doubt. The HRTEM image and its corresponding FFT pattern suggest that η′-phase has a hexagonal lattice with its *c*-parameter approximately equal to 6d_{111Al} (1.402 nm), which is the same as reported in Refs. [13, 19]. From Fig. 4c–e, the intensity change of (0002)$_{η′}$ and (0004)$_{η′}$ diffuse spots in FFT pattern indicates that the formation of an intact η′ phase must experience a long period of pregnancy, and the structure of η′ phase germinates in precipitates with a jump increasing in thickness from 7-atomic-layers to 10-atomic-layers in samples aged for 36 h. In the late stage of aging, a few of η-precursor precipitates have been observed as shown in Fig. 4f taken from the sample aged for 202 h. As boxed in Fig. 4f, the η-precursor has a hexagonal lattice with its *c*-parameter approximately equal to 4d_{111Al} (0.935 nm) and
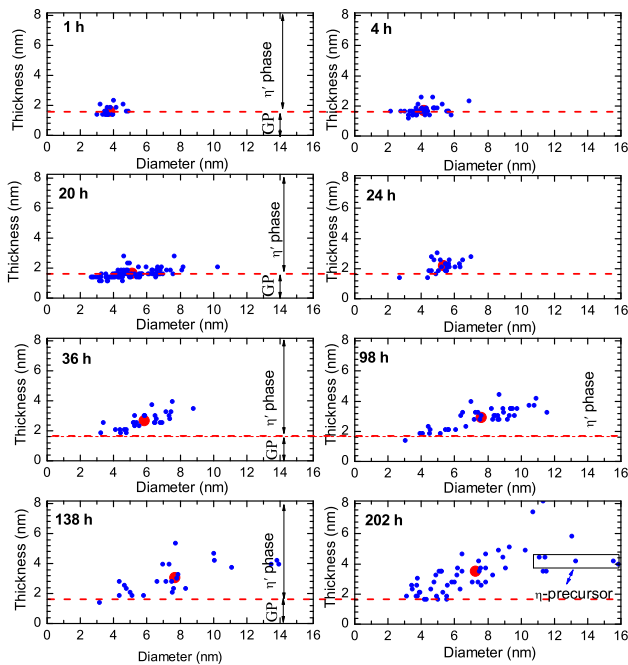
Fig. 7 Distribution of the thickness versus diameter of precipitates in samples with different aging times, the *red points* correspond to the average thickness and diameter of precipitates

$a = 0.496$ nm. Correspondingly, in the FFT pattern as inserted in Fig. 4f, the diffuse spots $(0002)_{\eta\text{-precursor}}$ on position of $1/2\ (111)_{Al}$ reciprocal vector become much stronger. No η-phases have been observed in the samples aged for less than 202 h.

Figure 5 shows HRTEM images of typical precipitates along $<112>_{Al}$ zone axis in the samples aged at 120 °C for different time. It further confirms the results summarized from Fig. 4. In the early stage of aging, i.e., in the samples aged for less than 20 h, GPII zones are mainly responsible for the strength of alloy, and grow up along with diameter but keep the same thickness, as shown in Fig. 5a, b. After aging for 36 h, a jump increasing in thickness of the precipitates induces phase transformation from GPII zones to η' phase. Then, η' precipitates grow along with thickness and diameter in turn as displayed in Fig. 5c–e. After reaching a certain thickness, η' precipitates grow faster along with the diameter. In the late stage of aging, a few η-precursor precipitates are also distinguished as in Fig. 5f.

In order to know the three-dimensional morphology of the precipitates, another observation is needed to be carried out along $<111>_{Al}$ zone axis, as shown in Fig. 6. Before 20 h, GPII zones are too thin to penetrate through the TEM sample, only strain field contrast is present. After 36 h aging, the projection of η' precipitates are all near circular. In the sample aged for 202 h, besides some ellipse η' precipitates, there are a few hexagonal η-precursor precipitates.

4 Discussion

4.1 Evolution of Precipitate Morphology

In order to know the size distribution of the precipitates, an enormous amount of statistic data was collected as exhibited in Fig. 7. At least 50 HRTEM images were analyzed. It can be seen that the diameter of the precipitates is larger and larger with increasing aging time to 20 h, but the thickness of the precipitates keeps constant in this stage. The sample aged for 20 h has the highest hardness, which is mainly contributed by GPII zones, which is suggested by the statistic data in Fig. 7. After 20 h aging, the thickness of the precipitates increases rapidly, which induces the phase transformation from GPII zones to η' phase (referring to the HRTEM results in Figs. 4, 5). After the phase transformation, precipitates grow along their diameter again. A few η-precursor precipitates are also observed in the late stage of aging. Statistic data show that the sizes of the precipitates become more dispersive. In order to abstract the rule of morphological evolution of the precipitates, the average size in each stage was calculated by averaging the thickness and diameter, respectively. The results are indicated by red spots in Fig. 7.

Precipitates with the average size were sorted out and displayed in Fig. 8. The left and middle columns are HRTEM images taken along $<110>_{Al}$ and $<112>_{Al}$ zone axes, respectively. The three-dimensional schematic, as shown as the right column, summarizes the evolution of the precipitates from the viewpoint of morphology. In the initial stage of aging, disk-like GPII zones with the same thickness form and contribute to the strength of alloy. Then, the increase of the thickness induces phase transformation from GPII zones to platelet-like η' precipitates. In the late stage of aging, a few of hexagonal η-precursor precipitates are observed to devote to parts of the strength of alloys.

4.2 Relationship Between Precipitate Size and Hardness of Alloy

To understand the relation between the hardness of alloy and the morphology of precipitates, the average aspect ratio (diameter–thickness ratio) of the precipitate is defined as
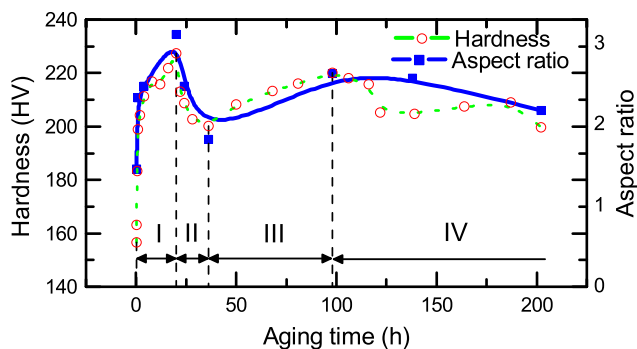
$$\overline{R} = \frac{\sum\limits_{1}^{N} \frac{d_i}{t_i}}{N},\qquad(1)$$

where N denotes the total number of the precipitates analyzed, d_i and t_i represent the diameter and the thickness of the precipitate i, respectively. The average aspect
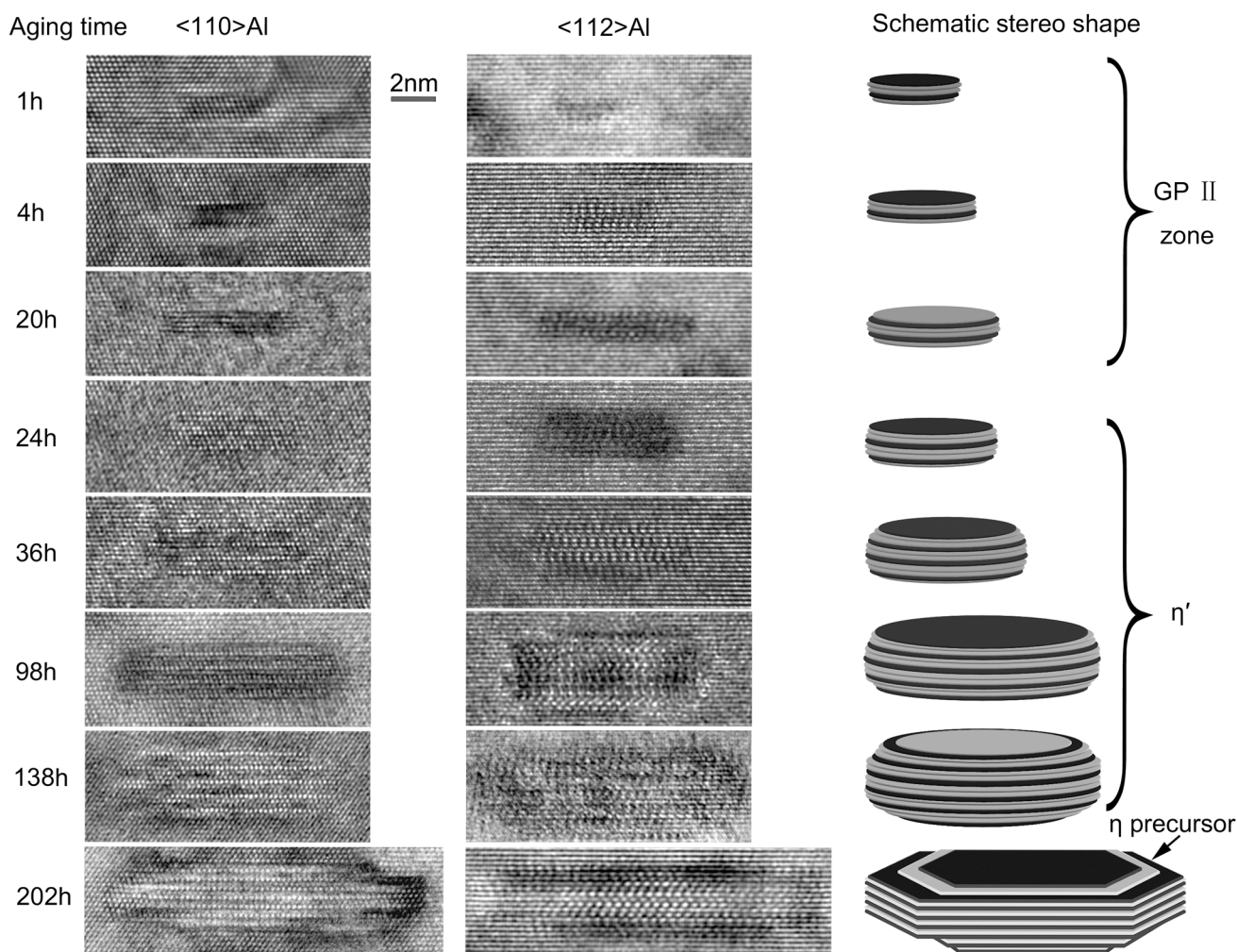
Fig. 8 Schematic of precipitate morphology changing along with aging time

Fig. 9 Comparison of the average aspect ratio–time curve with microhardness–time curve

ratio–time graph is plotted in Fig. 9, which matches well with the hardness–time graph. It reveals that the hardness values change along with the thickness–diameter ratios. Corresponding the hardness-aging curve, the average aspect ratio–time graph can be also roughly divided into four regions. In region I, the diameter–thickness ratio increases rapidly till the first peak reached, it is due to the fact that GPII zones with the same thickness nucleate and grow in diameter. In region II, after the first peak, the diameter–thickness ratio decreases with the hardness, since part of GPII zones transforms into thicker η′ phase. In region III, the diameter–thickness ratio increases slowly with hardness, because precipitates grow in thickness slower and in diameter faster (suggested by statistic data in Fig. 7). In region IV, after the second peak, the diameter–thickness ratio decreases slowly with the hardness, since some thicker η-precursor precipitates form and gobble up part of GPII zones (referring to the statistic data in Fig. 7).

4.3 Error Analysis

The error of analysis of the relationship between the precipitate size and the hardness mainly comes from two parts:

one is from the error of statistic and the other is from the intrinsic delocalization effect of HRTEM image. In order to measure the size of the precipitates more accurately, the precipitates must be observed by HRTEM due to their nano-size. However, the view field of an HRTEM image is limited. Moreover, just 50 images were selected to do statistic analysis with the limitation of workload. Hence, of course the statistic results have a certain margin of error. The delocalization of HRTEM images will obscure the interface of the precipitates and reduce the accuracy of measurement, although we optimize the defocus value to decrease the effect of delocalization as far as possible. This error may be eliminated by high angle annular dark field (HAADF) scanning transmission electron microscopy (STEM) technique [29].

5 Conclusion

The morphological evolution of the precipitates has been investigated by HRTEM based on statistic. It reveals that the hardness of the alloy changes accordingly with the change of the average thickness–diameter ratio of precipitates. GPII zones keep 7-atomic-layers in the thickness and grow along with the diameter. Once the thickness change, the phase transformation from GPII zones to η′ or η-precursor would occur. After η′ and η-precursor form, the precipitates grow along with the thickness slower and the diameter faster. The statistic data confirm that GPII zones are mainly responsible for the first and also the highest hardness peak of Al–7.4Zn–1.7Mg–2.0Cu (wt%) alloy at 120 °C. After the first hardness peak, the metastable η′ precipitates and η-precursor, coexisting with part of GPII zones, are counted as the main hardening precipitates.

References

[1] J.P. Immarigeon, R.T. Holt, A.K. Koul, L. Zhao, W. Wallace, J.C. Beddoes, Mater. Charact. **35**, 41 (1995)
[2] I.J. Polmear, Mater. Forum **28**, 1 (2004)
[3] G.Y. Lin, Z.F. Zhang, H. Zhang, D.S. Peng, J. Zhou, Acta Metall. Sin. (Engl. Lett.) **21**, 109 (2008)
[4] S. Devaraj, S. Sankaran, R. Kumar, Acta Metall. Sin. (Engl. Lett.) **26**, 761 (2013)
[5] S. Li, J. Zhang, J. Yang, Y. Deng, X. Zhang, Acta Metall. Sin. (Engl. Lett.) **27**, 107 (2014)
[6] H. Loffler, I. Kovacs, J. Lendvai, J. Mater. Sci. **18**, 2215 (1983)
[7] X. Li, B. Xiong, Y. Zhang, C. Hua, F. Wang, B. Zhu, H. Liu, Sci. China E **52**, 67 (2009)
[8] J. Chen, L. Zhen, S. Yang, W. Shao, S. Dai, Mater. Sci. Eng. **500**, 34 (2009)
[9] S.K. Maloney, K. Honob, I.J. Polmear, S.P. Ringer, Micron **32**, 741 (2001)
[10] R.A. Jeshvaghani, H. Zohdi, H.R. Shahverdi, M. Bozorg, S.M.M. Hadavi, Mater. Charact. **73**, 8 (2012)
[11] L. Berg, J. Gjønnes, V. Hansen, X. Li, M. Knutson-Wedel, G. Waterloo, D. Schryvers, L. Wallenberg, Acta Mater. **49**, 3443 (2001)
[12] S.K. Maloney, K. Hono, I.J. Polmear, S.P. Ringer, Scr. Mater. **41**, 1031 (1999)
[13] X. Li, V. Hansen, J. Gjønnes, L. Wallenberg, Acta Mater. **47**, 2651 (1999)
[14] C. Marioara, W. Lefebvre, S. Andersen, J. Friis, J. Mater. Sci. **48**, 3638 (2013)
[15] Y.Y. Li, L. Kovarik, P.J. Phillips, Y.F. Hsu, W.H. Wang, M.J. Mills, Philos. Mag. Lett. **92**, 166 (2012)
[16] A. Kverneland, V. Hansen, R. Vincent, K. Gjønnes, J. Gjønnes, Ultramicroscopy **106**, 492 (2006)
[17] X. Fan, D. Jiang, Q. Meng, Z. Lai, X. Zhang, Mater. Sci. Eng. A **427**, 130 (2006)
[18] B. Pucun, H. Xiaohu, Z. Xiuyun, Z. Chunwang, X. Yongming, Mater. Sci. Eng. **508**, 23 (2009)
[19] J.Z. Liu, J.H. Chen, X.B. Yang, S. Ren, C.L. Wu, H.Y. Xu, J. Zou, Scr. Mater. **63**, 1061 (2010)
[20] T. Marlaud, A. Deschamps, F. Bley, W. Lefebvre, B. Baroux, Acta Mater. **58**, 248 (2010)
[21] T. Marlaud, B. Malki, C. Henon, A. Deschamps, B. Baroux, Corros. Sci. **53**, 3139 (2011)
[22] T. Engdahl, V. Hansen, P.J. Warren, K. Stiller, Mater. Sci. Eng. **327**, 59 (2002)
[23] K. Stiller, P.J. Warren, V. Hansen, J. Angenete, J. Gjønnes, Mater. Sci. Eng. **270**, 55 (1999)
[24] G. Sha, A. Cerezo, Acta Mater. **52**, 4035 (2004)
[25] G. Sha, A. Cerezo, Surf. Interface Anal. **36**, 564 (2004)
[26] Z.H. Li, B.Q. Xiong, Y.A. Zhang, B.H. Zhu, F. Wang, H.W. Liu, Trans. Nonferrous Met. Soc. Chin. **18**, 40 (2008)
[27] P. Guyot, L. Cottignies, Acta Mater. **44**, 4161 (1996)
[28] J.F. Nie, Scr. Mater. **48**, 1009 (2003)
[29] Y. Xu, D. Xu, X. Shao, E.H. Han, Acta Metall. Sin. (Engl. Lett.) **26**, 217 (2013)